

The comparison of the state-of-the-art nucleon-nucleon potentials from phase shift to nuclear matter

Ke Nan and Hong Shen

School of Physics, Nankai University, Tianjin 300071, China

Jinniu Hu*

*School of Physics, Nankai University, Tianjin 300071, China and
Shenzhen Research Institute of Nankai University, Shenzhen 518083, China*

Ying Zhang

*Department of Physics, Faculty of Science,
Tianjin University, Tianjin 300072, China*

(Dated: October 2, 2024)

Abstract

The nucleon-nucleon (NN) potential is the residual interaction of the strong interaction in the low-energy region and is also the fundamental input to the study of atomic nuclei. Based on the non-perturbative properties of the quantum chromodynamics (QCD), NN potential is not yet directly accessible from QCD theory. Therefore, various models of NN interactions have been constructed based on Yukawa's meson exchange pictures since the 1930s, including one-boson-exchange models, coordinate operator models and chiral effective field models. Analysis of extensive NN scattering data has shown that the two-body nuclear force exhibits a short-range repulsion and intermediate-range attraction, and decays rapidly with increasing distance. A series of charge-dependent high-precision NN interactions have been further developed in the past thirty years, such as the AV18 potential, CD-Bonn potential, pvCD-Bonn potentials, and the chiral effective nuclear potentials with momentum expansion up to the fifth order. In this work, the phase shifts at different channels, the cross sections, the entanglement entropy in spin space, and the equations of state of symmetric nuclear matter and pure neutron matter from these high-precision NN interactions are calculated and systematically compared. It can be found that they have significant differences in the cases with high angular momentum, high laboratory energy, and high-density regions.

* hujinniu@nankai.edu.cn

I. INTRODUCTION

The nucleon-nucleon (NN) interaction is a fundamental aspect of nuclear physics, governing the intricate quantum behavior of protons and neutrons within atomic nuclei. An effective NN force must precisely represent various characteristics, including strong repulsion at short distances, strong attraction at intermediate ranges, and diminishing to zero at long distances. Additionally, it must conform to fundamental symmetries including spatial rotation invariance, translational invariance, and space reflection invariance [1, 2].

The NN interaction represents the residual effect of the strong interaction at the level of nucleons, which is governed by quantum chromodynamics (QCD) theory. Early models, like Yukawa's one-pion-exchange model, laid foundational groundwork [3]. In the 1960s, the introduction of heavy bosons aimed to resolve short-range and intermediate-range NN interaction challenges [4]. Subsequently, the Bonn University group developed a comprehensive meson exchange model, culminating in 1987 with its final version [5, 6].

By the 1990s, meticulous analysis of extensive NN scattering data revealed significant differences in proton-proton (pp) and neutron-proton (np) scattering phase shifts after removing the Coulomb interaction contributions, prompting further investigations into charge dependence in nuclear interactions [7].

Charge independence in isospin space remains invariant under any rotation, while violations of this symmetry constitute charge-dependent or charge independence breaking (CIB). Charge symmetry breaking (CSB) specifically refers to deviations under a 180° rotation about the y -axis in isospin space, where the positive z direction correlates to positive charge. Thus, CSB, represents a subset of charge dependence, where strong NN interaction CIB indicates differences in interactions among pp , np , and neutron-neutron (nn) pairs in the isospin $T = 1$ state, after eliminating electromagnetic influences.

Since then, several high-precision NN interaction models have been established, such as Reid93, Nijmegen93, Nijmegen I, Nijmegen II [7], AV18 [8], and CD-Bonn [9]. Additionally, the chiral NN potential, based on chiral perturbation theory, has played a pivotal role [10–23]. The relativistic versions of chiral potentials, developed by the Beihang group, extend from leading order to next-to-next-to-leading order [24–26]. These advancements provide a more accurate description of NN scattering phase shifts at equivalent chiral expansion orders, as well as the saturation properties of symmetric nuclear matter [27]. Recent

contributions from the Granada group have explored phase shifts with delta potentials, addressing associated uncertainties [28, 29]. While these potentials effectively reproduce NN scattering data, variations in phase shifts under high partial waves and momentum regimes warrant detailed comparison.

Over the past 20 years, significant advances have been achieved in understanding baryon-baryon interactions, particularly NN potentials, through lattice QCD simulations. These efforts have successfully captured many of the fundamental characteristics of NN potentials [30–35]. Moreover, recent work has aimed to connect earlier model-dependent NN potentials with results obtained from lattice QCD theory [36–39].

The scattering amplitude, which governs cross sections, differential cross sections, and spin polarization observables in NN scattering, are encapsulated by the S -matrix through partial wave expansion. This unitary S -matrix parameterization, reliant on phase shifts and mixing angles across angular momentum channels, accurately describes these observables [29], with most high-precision NN potentials achieving $\chi^2/N \sim 1$. Furthermore, detailed comparisons of cross sections across various input nucleon energies remain pertinent.

Recent discussions on NN scattering entanglement in spin space and Wigner symmetry within the framework of chiral effective field theory have invoked concepts from quantum information theory. For instance, np scattering entanglement potency in the S -channel correlates with phase shift distinctions at 1S_0 and 3S_1 channels [40–44]. NN potentials have also facilitated *ab initio* investigations into finite nuclei and infinite nuclear matter using methods such as the variational approach, the Brueckner-Hartree-Fock method, and the relativistic Brueckner-Hartree-Fock method [45–54].

This study compares 17 high-precision NN potentials encompassing AV18 [8], CD-Bonn [9], pvCD-Bonn [55], and chiral effective field [20, 22, 23]. With these potentials, we analyze the phase shifts, cross sections, entanglement potency, and nuclear matter equations of state across different laboratory energies and densities. This paper is structured as follows: Section II presents phase shift comparisons across the 17 NN potentials, Section III showcases their differential cross sections, Section IV details entanglement power calculations, and Section V explores equations of state for nuclear matter. Finally, Section VI concludes with a summary and implications.

II. NUCLEON-NUCLEON PHASE SHIFTS

The Lippmann-Schwinger equation can be directly applied to study NN scattering processes, which are equivalent to considering the scattering boundary conditions in the Schrödinger equation [9],

$$\left[\frac{d^2}{dr^2} + q^2 - \frac{l(l+1)}{r^2} - MV \right] \chi_l(r; q) = 0, \quad (1)$$

where, l is the orbital angular momentum, V is the NN interaction, and q is the momentum of the input particle. The asymptotic behavior of the radial wave function χ_l determines the scattering phase shift. If V is not a long-range force, the asymptotic wave function of χ_l is the Riccati-Bessel function.

The Lippmann-Schwinger equation introduces the T matrix, which can be expressed as an integral equation related to the interaction,

$$T(\vec{p}', \vec{p}) = V(\vec{p}', \vec{p}) + \int d^3\vec{k} V(\vec{p}', \vec{k}) \frac{1}{E - E_K + i\epsilon} T(\vec{k}, \vec{p}). \quad (2)$$

For computational convenience, we usually solve the Lippmann-Schwinger equation in the partial wave representation. In this representation, the T matrix and the interaction potential V can be expressed as,

$$\begin{aligned} T_{ll'}^{sj}(p', p) &= \langle p', l', s, j | T | p, l, s, j \rangle, \\ V_{ll'}^{sj}(p', p) &= \langle p', l', s, j | V | p, l, s, j \rangle. \end{aligned} \quad (3)$$

In NN scattering, the total angular momentum and total spin are conserved. Therefore, in the partial wave representation, the Lippmann-Schwinger equation can be formulated as,

$$T_{ll'}^{sj}(p', p) = V_{ll'}^{sj}(p', p) + \sum_{l''} \frac{2}{\pi} \int_0^\infty dk k^2 V_{ll''}^{sj}(p', k) \frac{1}{E - E_k + i\epsilon} T_{l''l'}^{sj}(k, p). \quad (4)$$

There are various methods for numerically solving the Lippmann-Schwinger equation, with one common approach being the matrix inversion method proposed by Haftel and Tabakin in 1970 [56]. This method employs Gaussian integration to transform the integral into a numerical summation, thereby converting the Lippmann-Schwinger equation into a matrix form,

$$T_{ll'}^{sj}(p', p) = V_{ll'}^{sj}(p', p) + \frac{2}{\pi} \sum_{l''} \sum_{i=1}^{N_p} w_i k_i^2 V_{ll''}^{sj}(p', k_i) \frac{2m}{p^2 - k_i^2 + i\epsilon} T_{l''l'}^{sj}(k_i, p), \quad (5)$$

where k_i and w_i represent momentum grid points and integration weights, respectively. In practical computations, Gauss-Legendre integration is frequently used. N_p is the number of momentum grid points, and with a sufficiently large N_p , numerical integration achieves high accuracy. By moving the part of Eq. (5) related to T to the left side, the matrix equation $(\mathbf{1} - \mathbf{V}\mathbf{G})\mathbf{T} = \mathbf{V}$ is obtained, and the T matrix is ultimately determined by matrix inversion: $\mathbf{T} = \mathbf{V}(\mathbf{1} - \mathbf{V}\mathbf{G})^{-1}$. However, it's worth noting that since the propagator $G = \frac{2m}{p^2 - k_i^2 + i\epsilon}$ contains complex terms, the resulting T matrix should be represented as complex numbers. To facilitate practical computation, a purely real R matrix is introduced. By defining the R matrix as,

$$R = T + i\pi T\delta(E + H_0)R, \quad (6)$$

the Lippmann-Schwinger equation can be expressed in a purely real form,

$$R(\vec{q}', \vec{q}) = V(\vec{q}', \vec{q}) + P \int d^3\vec{k} V(\vec{q}', \vec{k}) \frac{M}{q^2 - k^2} R(\vec{k}, \vec{q}). \quad (7)$$

This equation can be solved in partial wave representation similar to computing the T matrix. Once the R matrix is obtained, the phase shifts for the spin-singlet and non-coupled spin-triplet states can be written as:

$$\tan \delta_{jj}^{0j}(T_{lab}) = -\frac{\pi}{2} q M R_{jj}^{0j}(q, q), \quad (8)$$

$$\tan \delta_{jj}^{1j}(T_{lab}) = -\frac{\pi}{2} q M R_{jj}^{1j}(q, q). \quad (9)$$

Since there is a tensor component in the NN interaction, orbital angular momentum couples when $s = 1$. For such coupled states, a unitary matrix exists that diagonalizes the 2×2 R matrix. Thus, besides the phase shifts for the two coupled channels, there is a so-called mixing angle $\tilde{\epsilon}_j$. Typically, in NN scattering calculations, two labeling methods are commonly used. The first one, introduced by Blatt and Biedenharn [57], involves eigenphase shifts $\tilde{\delta}_{\mp}^j$ for the coupled channels, which can be expressed using the on-shell R matrix as,

$$\tan \tilde{\delta}_{\mp}^j = -\frac{\pi}{4} q M \left[R_{--}^j + R_{++}^j \pm \frac{R_{--}^j - R_{++}^j}{\cos 2\tilde{\epsilon}_j} \right]. \quad (10)$$

The mixing angle coefficient $\tilde{\epsilon}_j$ is given by:

$$\tan 2\tilde{\epsilon}_j(T_{lab}) = \frac{2R_{+-}^j}{R_{--}^j + R_{++}^j}. \quad (11)$$

All the R matrix elements in the above expressions are parameterized by (q', q) , where q is the on-shell momentum. The abbreviations used here are:

$$\begin{aligned} R_{++}^j &= R_{j+1, j+1}^{1j}, & R_{--}^j &= R_{j-1, j-1}^{1j}, \\ R_{+-}^j &= R_{j+1, j-1}^{1j}, & R_{-+}^j &= R_{j-1, j+1}^{1j}. \end{aligned} \quad (12)$$

Since the distinction between protons and neutrons is crucial for high-precision nuclear forces, it's necessary to consider this distinction in pp , nn , and np scattering. For pp scattering, the relation between on-shell momentum q^2 and nucleon mass M is:

$$q^2 = \frac{1}{2}M_p T_{lab}, \quad M = M_p, \quad (13)$$

for nn scattering:

$$q^2 = \frac{1}{2}M_n T_{lab}, \quad M = M_n, \quad (14)$$

and for np scattering:

$$q^2 = \frac{M_p^2 T_{lab} (T_{lab} + 2M_n)}{(M_p + M_n)^2 + 2T_{lab} M_p}, \quad M = \frac{2M_p M_n}{M_p + M_n}. \quad (15)$$

Here $M = M_p$ represents the proton mass, $M = M_n$ for the neutron mass, and T_{lab} is the kinetic energy of the incident particle in the laboratory system, its relation with q^2 is based on relativistic kinematics. Another representation of NN scattering phase shifts is proposed by Stapp et al [58]. Here, ϵ_j and δ^j are used, which are related to the Blatt-Biedenharn phase shifts as:

$$\begin{aligned} \delta_+^j + \delta_-^j &= \tilde{\delta}_+^j + \tilde{\delta}_-^j, \\ \sin(\delta_-^j - \delta_+^j) &= \tan 2\epsilon_j / \tan 2\tilde{\epsilon}_j, \\ \sin(\tilde{\delta}_-^j - \tilde{\delta}_+^j) &= \sin 2\epsilon_j / \sin 2\tilde{\epsilon}_j. \end{aligned} \quad (16)$$

These expressions consider only NN interaction and are suitable for nn and np scattering. For pp scattering, the Coulomb interaction needs to be taken into account.

The Lippmann-Schwinger equation is numerically solved using the matrix inversion method. A total of 6 sets (17 types) of high-precision realistic nuclear forces are calculated for various partial waves with laboratory incident energies less than 300 MeV and total angular momentum $j \leq 3$. The 6 sets of high-precision realistic nuclear forces are: the AV18 potential [8], which depends on spin-isospin operators in coordinate space; the CD-Bonn

potential, based on the one-boson exchange model with charge dependence [9]; the pvCD-Bonn potential, which considers pseudovector coupling between pion and nucleon based on the CD-Bonn potential [55]; and three sets of chiral nuclear forces derived from chiral effective field theory, up to fifth-order momentum perturbation effects (N⁴LO) [20, 22, 23]. The differences among these chiral nuclear forces mainly lie in the power counting rules for perturbation orders, the form of regularization factors, and the slightly different cutoff constants. Of course, the uncertainties arising from different expansion orders in the chiral potentials are very important. Various methods to estimate these uncertainties are discussed in Refs. [20, 22, 59–61]. In this work, we focus on comparing the high-precision NN potentials from different theoretical frameworks. Thus, we will not include the uncertainties of chiral forces on phase shifts, cross sections, and so on in the results.

All aforementioned high-precision realistic nuclear forces effectively reproduce experimental scattering data, achieving an accuracy of $\chi^2/N \sim 1$. Throughout our calculations, we meticulously consider the isospin effects of nucleon scattering, categorizing them into pp , nn , and np channels. Among these, experimental pp scattering data currently boasts the highest accuracy, while nn scattering data remains relatively sparse. We will sequentially present our computed results and analysis of phase shifts for np , nn , and pp channels using the aforementioned high-precision nuclear forces.

In Fig. 1, we present the np scattering phase shifts for the isospin $T = 1$ channel calculated using 17 types of high-precision NN interactions. These include AV18 [8], CD-Bonn [9], pvCD-Bonn A, B, C [55], N⁴LO 450(EMN), N⁴LO 500(EMN), N⁴LO 550(EMN) [22], N⁴LO 0.8(EKM), N⁴LO 0.9(EKM), N⁴LO 1.0(EKM), N⁴LO 1.1(EKM), N⁴LO 1.2(EKM) [20], N⁴LO 400(RKE), N⁴LO 450(RKE), N⁴LO 500(RKE), and N⁴LO 550(RKE) [23] potentials. Additionally, to compare with experimental data, we also include the phase shift values obtained by the Nijmegen group in 1993 through partial wave analysis (PWA93) [7] of scattering data.

For the 1S_0 channel, within the incident energy range up to $E \leq 300$ MeV, except for the chiral force N⁴LO 450(EMN) from the Idaho group, the phase shifts obtained from the other 16 high-precision nuclear forces are consistent, and they match completely with the PWA93 data. At $E \geq 200$ MeV, the deviation of the 1S_0 phase shift from N⁴LO 450(EMN) compared to other potentials should mainly stem from the smaller cutoff value Λ . For channels with $l \leq 2$, such as 3P_0 , 3P_1 , 1D_2 , and 3P_2 , all high-precision nuclear forces yield

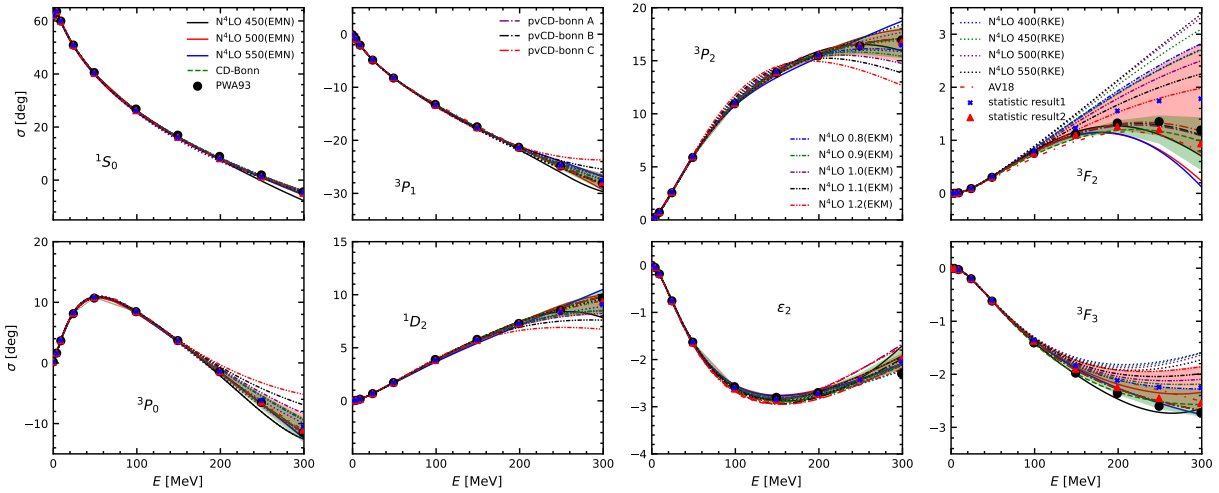


FIG. 1. The variation of scattering phase shifts with incident energy for np ($T = 1$) channels calculated by various high-precision nuclear forces with $J \leq 3$, along with statistical error analysis.

essentially identical phase shift values at $E \leq 200$ MeV. As the incident energy increases, deviations in the phase shifts computed using chiral forces begin to appear, which are also related to their smaller cutoff values. In 3F_2 and 3F_3 channels, these deviations are further amplified. Only when $E \leq 100$ MeV, the phase shift values from the 17 potentials are relatively close. This is because in chiral effective theory, for $N^4\text{LO}$ forces, the attempt to fit the experimental values for low-energy couplings is truncated only to the 3D_3 channel, so the phase shift values for 3F_2 and 3F_3 channels can only be regarded as theoretical predictions. Thus, various counting rules for different perturbation orders and cutoff momenta may affect the phase shift values for these two channels.

We assume that the phase shifts generated by these potentials at each incident energy point follow a Gaussian distribution,

$$X \sim \mathcal{N}(\mu, \sigma^2) = \frac{1}{\sigma\sqrt{2\pi}} e^{-\left(\frac{x-\mu}{\sigma}\right)^2}, \quad (17)$$

where μ is the mean value and σ is the standard deviation. Therefore, we can consider $\mu \pm \sigma$ as the central value and its deviation for theoretical phase shift calculations. The shaded areas in Fig. 1 represent these results. Due to significant discrepancies between the predictions of many chiral forces and the results of partial wave analysis in describing F -channel phase shifts, when performing statistical analysis on the theoretical phase shift results, we selected two groups of potentials: the first group includes all 17 potentials (shaded in red), while

the second group excludes the 9 potentials from N⁴LO (EKM) and N⁴LO (RKE) (shaded in green).

We found that for channels with $l < 3$, the choice of potential sets had minimal impact on the final central values and standard deviations. However, for the F -wave channels, excluding the results from the EKM and RKE sets of chiral nuclear forces significantly reduced the standard deviation of the second group, and the central values remained consistent with the results from PWA93. Therefore, caution should be exercised when using the results from these two sets of chiral nuclear forces, especially for energies greater than 200 MeV. Particularly, for the P -wave and D -wave channels, significant discrepancies were observed at higher incident energies compared to the results obtained with other potential sets, especially when the truncation length of the EKM potential is relatively large.

E/MeV	PWA93	N ⁴ LO500 (EMN)	CD-Bonn	pvCD-Bonn B	N ⁴ LO1.0 (EKM)	N ⁴ LO400 (RKE)	AV18	Analysis
1	62.07	62.03	62.11	62.13	62.10	62.07	61.80	62.07±0.07
5	63.63	63.47	63.68	63.69	63.65	63.58	63.39	63.61±0.08
10	59.96	59.72	60.01	60.02	59.97	59.86	59.69	59.92±0.10
25	50.90	50.47	50.93	50.93	50.90	50.66	50.55	50.80±0.14
50	40.54	39.82	40.44	40.43	40.43	39.99	40.03	40.30±0.20
100	26.78	25.66	26.37	26.32	26.34	25.50	25.97	26.19±0.30
150	16.94	15.76	16.30	16.24	16.22	15.17	15.94	16.11±0.36
200	8.94	7.88	8.29	8.23	8.15	7.15	7.95	8.06±0.37
250	1.96	0.93	1.56	1.51	1.41	0.77	1.24	1.27±0.48
300	-4.46	-5.60	-4.28	-4.31	-4.35	-4.31	-4.58	-4.62±0.84

TABLE I. The phase shifts of various interaction potentials in the np 1S_0 channel, along with their averages and statistical error analysis.

In Table I, we present specific values of scattering phase shifts obtained by various typical np interaction potentials in the 1S_0 channel at different incident energies. The values in the second column are derived from the partial wave analysis PWA93. The intermediate columns correspond to the results obtained from N⁴LO 500(EMN), CD-Bonn, pvCD-Bonn B, N⁴LO 1.0(EKM), N⁴LO 400(RKE), and AV18 potentials, respectively. The last column represents the central values and deviations of the phase shifts obtained using Gaussian distribution for all 17 potentials. The deviations are relatively small at lower incident energies but gradually increase with energy. Particularly, the scattering phase shift of N⁴LO 500(EMN)

at an incident energy of 300 MeV is significantly smaller than that of other potentials. This results in a slightly smaller central value obtained through statistical analysis compared to the data from PWA93. However, considering the effect of deviations, this result is reasonable.

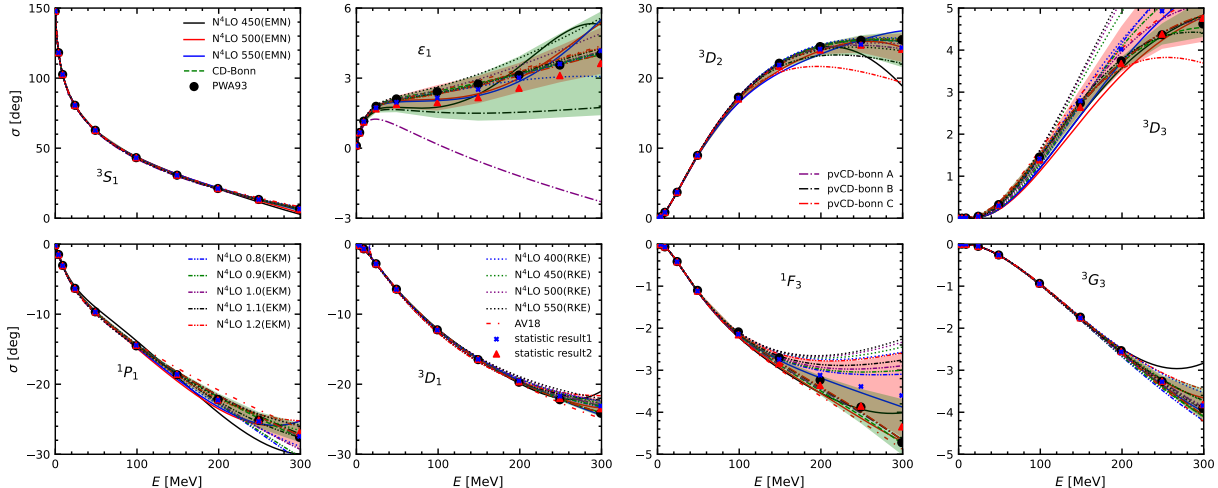


FIG. 2. The np ($T = 0$) channel's phase shift as a function of incident energy, computed by various high-precision nuclear forces for $j \leq 3$, along with a statistical error analysis, is depicted in the graph.

In np interactions, besides the isovector channel ($T = 1$), there is also the case of the isoscalar channel ($T = 0$). Nuclear potentials involve a strong tensor force component, primarily manifested in the mixing effect of the 3S_1 and 3D_1 channels in np interactions. This is closely related to the mixing angle ε_1 . The nuclear force in the 3S_1 channel exhibits attraction throughout the entire range of incident energies, with phase shift values obtained from various interactions being essentially consistent. However, for other channels, as the incident energy increases, differences in the phase shift values calculated by various high-precision nuclear forces become increasingly apparent, especially when the incident energy exceeds 100 MeV. The differences in the mixing angles ε_1 calculated by these nuclear forces are also significant, indicating variations in their tensor components. For instance, the trend of the mixing angle ε_1 for the pvCD-Bonn A potential changes opposite to other potentials as the energy increases, showing an initial increase followed by a decrease. For $j = 3$ channels, the computed values from various chiral nuclear forces significantly deviate from the PWA93 partial wave analysis. Therefore, when conducting statistical analysis on the phase shifts generated by these potentials, we adopt the same approach as for the isovector $T = 1$ case.

E/MeV	PWA93	N ⁴ LO500(EMN)	CD-Bonn	pvCD-Bonn	B N ⁴ LO1.0(EKM)	N ⁴ LO400(RKE)	AV18	Analysis
1	147.75	147.74	147.74	147.76	147.75	147.74	148.00	147.75±0.06
5	118.18	118.17	118.17	118.20	118.18	118.15	118.52	118.18±0.09
10	102.61	102.60	102.61	102.63	102.61	102.56	102.94	102.60±0.10
25	80.63	80.64	80.62	80.63	80.60	80.50	80.93	80.60±0.13
50	62.77	62.89	62.71	62.70	62.71	62.49	63.08	62.71±0.19
100	43.23	43.70	43.05	43.02	43.13	42.68	43.65	43.16±0.36
150	30.72	31.40	30.44	30.43	30.64	30.11	31.31	30.67±0.42
200	21.22	21.58	20.93	20.93	21.20	20.87	22.04	21.18±0.33
250	13.39	12.65	13.19	13.22	13.52	13.70	14.54	13.36±0.57
300	6.60	3.98	6.62	6.68	7.04	8.05	8.21	6.66±1.30

TABLE II. The np 3S_1 channel: phase shifts of various interaction potentials and their average values with statistical error analysis.

One approach considers all phase shifts generated by interactions, while the other excludes the N⁴LO(EKM) and N⁴LO(RKE) series of chiral forces. The latter approach yields phase shift center values that are generally closer to the results of the PWA93 partial wave analysis.

Table II presents the numerical values of phase shifts for various interaction potentials in the np 3S_1 channel, ranging from 1 MeV to 300 MeV of incident nucleon energy. The last column displays the phase shift values calculated considering all potential fields, along with the average phase shift obtained through statistical analysis and the corresponding statistical error at different energies. The positive phase shift values in the 3S_1 channel within this energy range indicate strong attractive interactions between nucleons. At energies below 200 MeV, the phase shift values computed by various high-precision nuclear forces are generally consistent with the results of the PWA93. However, as the energy increases, deviations gradually appear in the results for different interactions, with the N⁴LO 500(EMN) potential showing the largest discrepancy. From Table II, it can be observed that the central value at 5 MeV incident nucleon energy is 147.75 with a deviation of 0.06, at 100 MeV it is 43.16 with a deviation of 0.36, and at 300 MeV it is 6.66 with a deviation of 1.30.

Since neutrons are charge neutral, there is currently very little experimental data on nn scattering, so there are no results from phase shift analyses. However, the charge-independent symmetry of nuclear forces has a weak breaking, so there is only a slight difference between the scattering phase shifts of nn and np channels in the $T = 1$ channel.

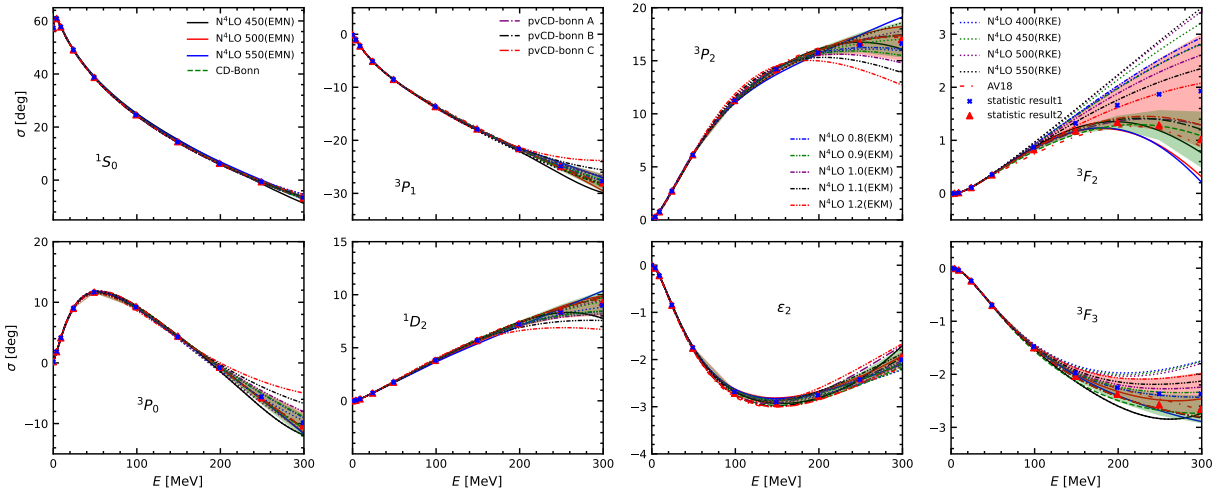


FIG. 3. The variation of scattering phase shifts with incident energy for nn ($T = 1$) channels calculated by various high-precision nuclear forces with $J \leq 3$, along with statistical error analysis.

Especially at lower incident energies, due to the Pauli exclusion principle, the attractive strength of nn interaction is slightly smaller compared to the np interaction in the 1S_0 channel.

In Fig. 3, the phase shifts of nn scattering from 17 types of high-precision nuclear potentials are shown with the corresponding statistical mean values and deviations. They have quite similar tendencies to those of np scattering. Table III lists the 1S_0 channel shifts calculated using $N^4\text{LO } 500(\text{EMN})$, CD-Bonn , pvCD-Bonn B , $N^4\text{LO } 1.0(\text{EKM})$, $N^4\text{LO } 400(\text{RKE})$, and AV18 potentials. It can be observed that the range of shifts in the 1S_0 channel is from 60 to -7 . The shifts from 1 MeV to 50 MeV within the range of nucleon incident energy are consistent across various potentials. However, deviations between different potentials calculated after 100 MeV gradually increase, with $N^4\text{LO } 1.0(\text{EKM})$ having the largest deviation, while the others have relatively small deviations.

Fig. 4 presents the pp channel scattering cases with the same potentials as the nn and np cases. For pp potential, a Coulomb repulsive interaction should be considered. Therefore, the phase shifts of pp scattering are reduced at low incident energy regions compared to those of nn and np scattering. The Coulomb force is a long-range interaction, which has small influence on the high-energy scattering region. These high-precision nucleon potentials exhibit similar behaviors as in the nn and np cases.

Table IV presents the phase shifts in the pp 1S_0 channel. It can be observed from the

E/MeV	$N^4\text{LO}500(\text{EMN})$	CD-Bonn	pvCD-Bonn B	$N^4\text{LO}1.0(\text{EKM})$	$N^4\text{LO}400(\text{RKE})$	AV18	Analysis
1	57.48	57.48	57.25	57.36	57.45	57.49	57.40 ± 0.09
5	60.94	60.92	60.83	60.88	60.98	60.88	60.91 ± 0.06
10	57.78	57.74	57.69	57.73	57.84	57.67	57.76 ± 0.07
25	49.08	49.02	49.03	49.07	49.19	48.94	49.10 ± 0.10
50	38.70	38.60	38.64	38.70	38.78	38.59	38.73 ± 0.14
100	24.65	24.38	24.44	24.50	24.45	24.55	24.58 ± 0.24
150	14.71	14.14	14.21	14.24	14.15	14.48	14.39 ± 0.32
200	6.76	5.97	6.06	6.05	6.15	6.44	6.24 ± 0.30
250	-0.26	-0.91	-0.79	-0.79	-0.22	-0.33	-0.63 ± 0.35
300	-6.85	-6.88	-6.74	-6.60	-5.29	-6.21	-6.57 ± 0.73

TABLE III. The phase shifts of various interaction potentials in the nn 1S_0 channel, along with their averages and statistical error analysis.

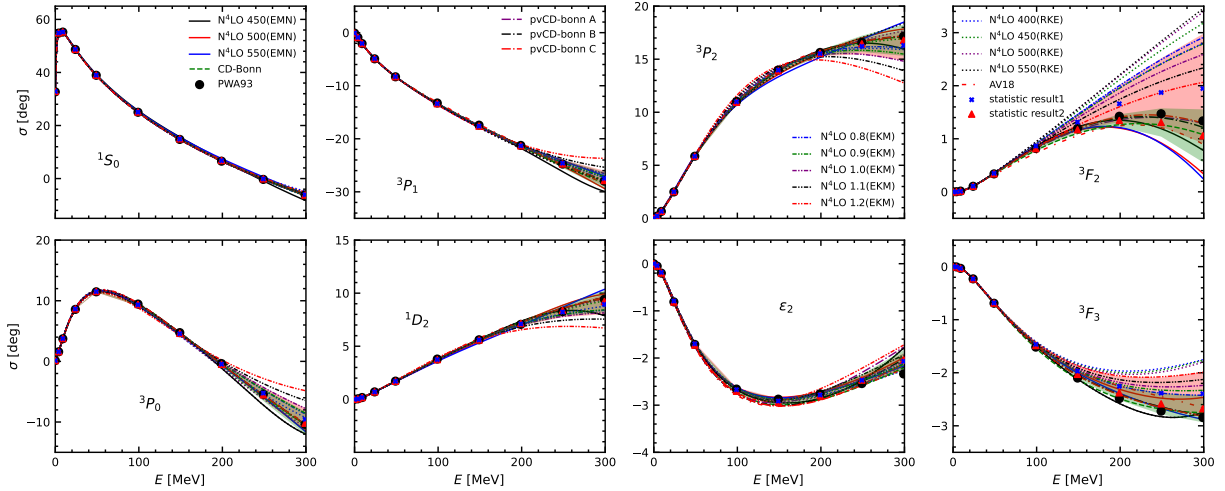


FIG. 4. The variation of scattering phase shifts with incident energy for pp ($T = 1$) channels calculated by various high-precision nuclear forces with $J \leq 2$, along with statistical error analysis.

table that the range of shifts in the 1S_0 channel is from 56 to -7 in the incident energy range from 1 MeV to 100 MeV. However, deviations gradually increase as the energy rises, with $N^4\text{LO} 500(\text{EMN})$ having the largest deviation, while others are closer to the mean values. According to the central value and deviation calculations, at 5 MeV, the central value is 54.91 with a deviation of 0.05, at 100 MeV, the central value is 25.06 with a deviation of 0.2, and at 300 MeV, the central value is -6.07 with a deviation of 0.73. The uncertainties from these potentials in the pp channel are smallest.

E/MeV	PWA93	N ⁴ LO500(EMN)	CD-Bonn	pvCD-Bonn	B N ⁴ LO1.0(EKM)	N ⁴ LO400(RKE)	AV18	Analysis
1	32.68	32.88	32.88	32.88	32.79	32.79	32.88	32.83±0.06
5	54.83	54.93	54.93	54.95	54.86	54.92	54.88	54.91±0.05
10	55.22	55.26	55.27	55.30	55.22	55.32	55.17	55.27±0.06
25	48.67	48.66	48.67	48.72	48.68	48.82	48.56	48.72±0.09
50	38.93	38.86	38.89	38.94	38.94	39.07	38.84	38.98±0.12
100	24.99	24.99	24.92	24.97	24.98	25.00	25.06	25.06±0.20
150	14.76	15.06	14.74	14.78	14.75	14.74	15.04	14.90±0.28
200	6.55	7.11	6.59	6.63	6.56	6.73	7.03	6.76±0.28
250	-0.31	0.11	-0.28	-0.23	-0.29	0.33	0.27	-0.12±0.35
300	-6.15	-6.44	-6.25	-6.18	-6.15	-4.79	-5.61	-6.07±0.73

TABLE IV. The phase shifts of various interaction potentials in the pp 1S_0 channel, along with their averages and statistical error analysis.

III. THE CROSS SECTION OF NUCLEON-NUCLEON SCATTERING

Once the phase shifts are obtained, the S matrix related to the scattering amplitude can be constructed as for the uncoupled channels $l = l' = j$ [29],

$$S_{ll'}^{sj} = e^{2i\delta_{jj}^{sj}}, \quad (18)$$

and for the coupled channels $l = j \pm 1$, $l' = j \pm 1$,

$$S_{ll'}^{sj} = \begin{pmatrix} e^{2i\delta_-^j} \cos 2\epsilon_j & ie^{i(\delta_-^j + \delta_+^j)} \sin 2\epsilon_j \\ ie^{i(\delta_-^j + \delta_+^j)} \sin 2\epsilon_j & e^{2i\delta_+^j} \cos 2\epsilon_j \end{pmatrix}. \quad (19)$$

The corresponding scattering amplitude for the NN system at the scattering angle θ is

$$M_{m',m}^s(\theta) = \frac{1}{2ik} \sum_{j,l',l} i^{l-l'} \sqrt{4\pi(2l+1)} Y_{l',m'-m}(\theta, 0) C(l'js|m-m', m') C(ljs|0, m, m) (S_{ll'}^{sj} - \delta_{l',l}), \quad (20)$$

where C is the Clebsch-Gordan coefficients. This scattering amplitude is given in the spin-coupled representation, whereas it is more convenient to show it in the helicity basis for describing the NN scattering observables,

$$M_{m'_1, m'_2, m_1, m_2} = \sum_{m, m', s, s'} C\left(\frac{1}{2} \frac{1}{2} s | m_1, m_2, m\right) C\left(\frac{1}{2} \frac{1}{2} s | m'_1, m'_2, m'\right) M_{m, m'}^s. \quad (21)$$

$m_1, m_2, m'_1, m'_2 = \pm\frac{1}{2}$ are the third spin components of input and scattering nucleons, respectively. Therefore, the scattering amplitude is a 4×4 matrix for the NN system. Due to the parity and time-reversal symmetries, there are only 5 independent complex components in this matrix, which can be parameterized. Many attempts and notations were developed for this parameterization process [62–64]. A traditional definition is the Wolfenstein scheme [62],

$$M(\hat{k}_f, \hat{k}_i) = a + m(\sigma_1 \cdot \vec{n})(\sigma_2 \cdot \vec{n}) + (g - h)(\sigma_1 \cdot \vec{m})(\sigma_2 \cdot \vec{m}) \\ + (g + h)(\sigma_1 \cdot \vec{l})(\sigma_2 \cdot \vec{l}) + c(\sigma_1 + \sigma_2) \cdot \vec{n} \quad (22)$$

where, $\vec{n}, \vec{m}, \vec{l}$ are the three unitary vectors along the directions of $\vec{k}_f \perp \vec{k}_i$, $\vec{k}_f - \vec{k}_i$, and $\vec{k}_f + \vec{k}_i$.

For the spin-unpolarized input and scattering states, the differential cross section of NN scattering can be presented by these five Wolfenstein parameters,

$$\frac{d\sigma}{d\Omega} = \frac{1}{4} \sum_{m'_1, m'_2, m_1, m_2} |M_{m'_1, m'_2, m_1, m_2}(\hat{k}_f, \hat{k}_i)|^2 = \frac{1}{4} \text{Tr} [MM^\dagger] \\ = |a|^2 + |m|^2 + 2|c|^2 + 2|g|^2 + 2|h|^2. \quad (23)$$

The spin-polarized observables can also be derived with the spin density matrix operator and its polarization projection operator.

Once the phase shifts at different partial wave channels are obtained, the scattering observables can be generated by the scattering amplitude given by Eq. (20). It was parameterized as a, c, m, g, h by the Wolfenstein scheme. In the present work, the differential cross sections $d\sigma/d\Omega$ in Eq. (23) from different potentials are evaluated, where the angular partial waves must be included up to $j = 20$.

In Fig. 5, the differential cross section as a function of center-of-mass scattering angle with laboratory energies at $E_{lab} = 50$ MeV and $E_{lab} = 96$ MeV are plotted. The corresponding experimental data are compared. The 17 types of high-precision nuclear potentials provide the identical differential cross section at $E_{lab} = 50$ MeV, which is consistent with the experimental data very well. When the E_{lab} grows up to 96 MeV, the results from N⁴LO 500(EMN) and pvCD-Bonn A have significant differences from other calculations. The $d\sigma/d\Omega$ at small θ_{cm} of N⁴LO 500(EMN) becomes lower. The one from pvCD-Bonn A reduces round $\theta_{cm} = 90$ and is closer to the experimental data, whose mixing angle has a distinct behavior compared to other potentials.

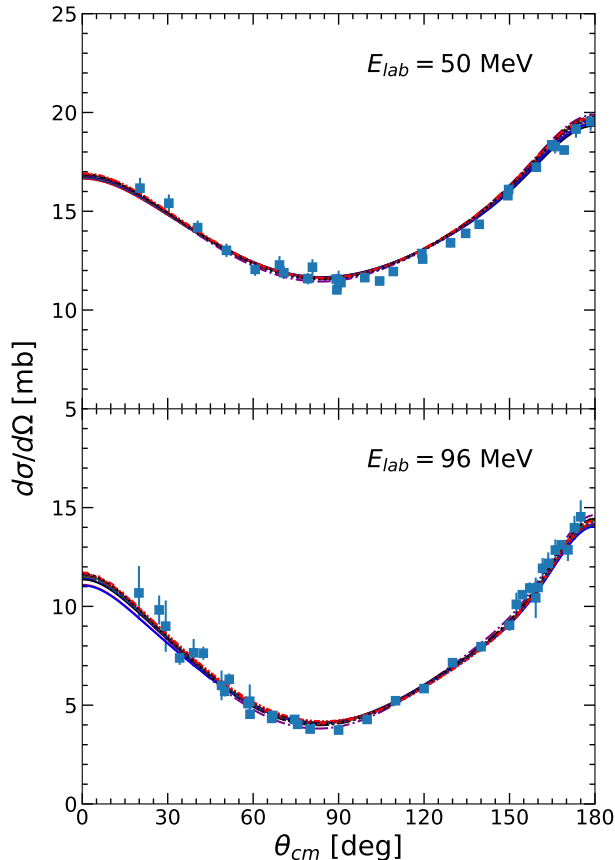


FIG. 5. The differential cross sections for pp scattering calculated by various high-precision nuclear forces with incident energies, $E_{lab} = 50$ MeV and $E_{lab} = 96$ MeV. The meanings of line styles are same as Fig. 4.

With the incident energy increment, the discrepancies in $d\sigma/d\Omega$ from these potentials more pronounced. In Fig. 6, the differential cross sections for pp scattering with $E_{lab} = 212$ MeV and $E_{lab} = 284$ MeV at different scattering angles are given. The chiral potentials, which do not accurately describe the F channels, exhibit significant deviations from experimental data at both forward and backward scattering angles. This is due to the construction of the S -matrix based on phase shifts. At higher collision energies, the convergence of the momentum expansion for chiral potentials deteriorates.

IV. ENTANGLEMENTS OF THE NUCLEON-NUCLEON SCATTERING

The entanglement of identical particles perfectly exhibits the nonlocality of quantum mechanics and has attracted numerous interesting investigations in the field of quantum

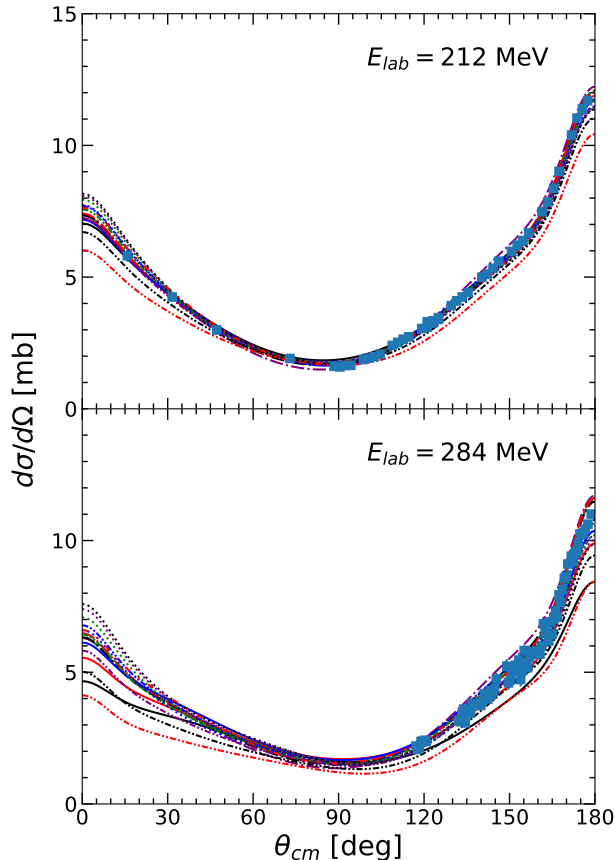


FIG. 6. The differential cross sections for pp scattering calculated by various high-precision nuclear forces with incident energies, $E_{lab} = 212$ MeV and $E_{lab} = 284$ MeV. The meanings of line styles are same as Fig. 4.

information in the past decades. Recently, it was applied to study the Wigner $SU(4)$ symmetry in the strong interaction from the perspective of NN scattering in the framework of chiral effective field theory. An entanglement power of S matrix was defined to describe the averaged entanglement ability of the scattering matrix by considering all initial states [41],

$$\varepsilon(\hat{S}) = 1 - \int \frac{d\Omega_1}{4\pi} \frac{d\Omega_2}{4\pi} \text{Tr}_1[\hat{\rho}_1^2]. \quad (24)$$

Here, $\hat{\rho}_1$ is a reduced density matrix for the nucleon 1 in the spin space which can be obtained from the two-nucleon density matrix $\hat{\rho}_{12}$,

$$\hat{\rho}_1 = \text{Tr}_2(\hat{\rho}_{12}) = \text{Tr}_2(|\psi_{\text{out}}\rangle\langle\psi_{\text{out}}|). \quad (25)$$

The scattering state $|\psi_{\text{out}}\rangle$ is generated by the initial state and S matrix,

$$|\psi_{\text{out}}\rangle = \hat{S}|\psi_{\text{in}}\rangle. \quad (26)$$

The initial state can be represented by two angles in the spherical coordinate,

$$|\psi_{\text{in}}\rangle = \left(\cos \frac{\theta_1}{2}, \exp(i\phi_1) \sin \frac{\theta_1}{2} \right)^T \otimes \left(\cos \frac{\theta_2}{2}, \exp(i\phi_2) \sin \frac{\theta_2}{2} \right)^T, \quad (27)$$

where $d\Omega_1 = \sin \theta_1 d\theta_1 d\phi_1$, $d\Omega_2 = \sin \theta_2 d\theta_2 d\phi_2$ and $\theta_1, \theta_2 \in [0, \pi]$, $\phi_1, \phi_2 \in [0, 2\pi]$. In the $l = 0$ channel, the S -matrix is decomposed into the 1S_0 and 3S_1 channel, if the mixing angle between 3S_1 and 3D_1 is neglected. The S -matrix can be denoted as the phase shifts at singlet and triplet channels, δ_0 and δ_1 ,

$$\hat{S} = \frac{1}{4}(e^{2i\delta_0} + 3e^{2i\delta_1})\mathbf{1} - \frac{1}{4}(e^{2i\delta_0} - e^{2i\delta_1})\vec{\sigma}_1 \otimes \vec{\sigma}_2. \quad (28)$$

Therefore, the density matrix $\hat{\rho}_{12}$ in the spin space is 4×4 . Its reduced density matrix for the nucleon 1 is reduced as 2×2 . The function $\text{Tr}_1[\hat{\rho}_1^2]$ is just related to $\theta_1, \theta_2, \phi_1$ and ϕ_2 . The entanglement power can be analytically written as,

$$\varepsilon(\hat{S}) = \frac{1}{6} \sin^2[2(\delta_1 - \delta_0)]. \quad (29)$$

The wave function of np scattering at tripled state $S = 1$ can be considered as an entanglement state in the spin space. An entanglement power about S -matrix can be evaluated through the two-body scattering wave function, which can be represented by the phase shifts at singlet and triplet channels, δ_0 and δ_1 if the mixing angle ε_1 is neglected. In the Fig. 7, the entanglement powers $\varepsilon(\hat{\mathcal{E}})$ from 17 high precision NN potentials are plotted and compared to that from PWA93. All of them equal *zero* around input momentum $p = 19.4$ MeV, where the phase shifts have a difference with $\pi/2$ between singlet and triplet channels and $|n \uparrow, p \downarrow\rangle$ converts into $|n \downarrow, p \uparrow\rangle$. At p around 90 MeV, the magnitude of entanglement power reaches the maximum value and then slowly reduces. The differences of $\varepsilon(\hat{\mathcal{E}})$ among 17 potentials start to become obvious after their peak values. In the intermediate momentum region, the entanglement from pvCD-Bonn A potential has the minimum value and is most consistent with that from the partial wave analysis of experimental data. When p approaches 400 MeV, the $\varepsilon(\hat{\mathcal{E}})$ from N⁴LO 500(EMN) shows a distinct difference compared to other potentials, since from Table II, its phase shifts at np 3S_1 channel are smaller than other one at high input energy region. Overall, the entanglement powers from the current high-precision NN potentials show very small differences, as the phase shifts for the 1S_0 and 3S_1 states of NN system are well-determined. In contrast, in other two-baryon systems, such as Σ^+p or Λp , the entanglement powers from different baryon-baryon potentials exhibit

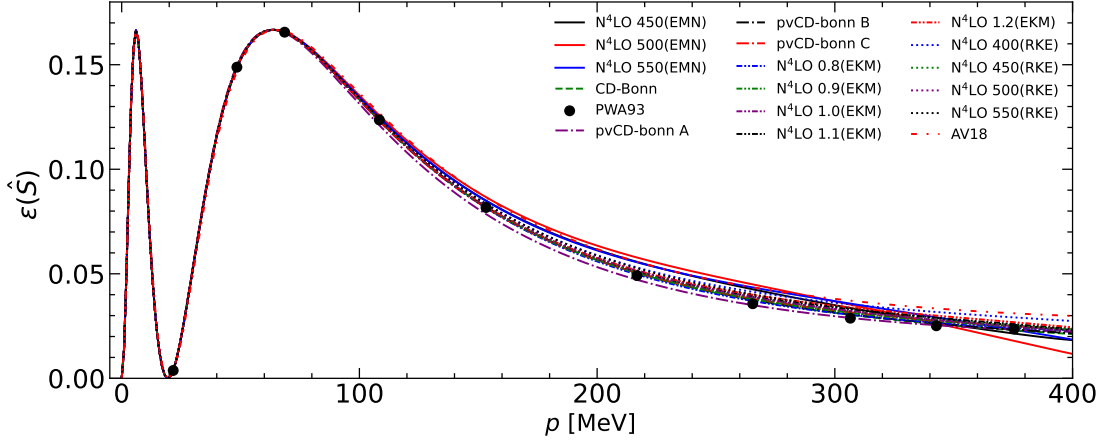


FIG. 7. The entanglement power at $l = 0$ channels from different high precision NN potentials. These results are compared to those from PWA93.

distinct behaviors [65]. Furthermore, the spin entanglement can be detected by measuring the spin polarizations of one nucleon in three directions during polarization experiments, which relates to the spin correlation parameters [66].

V. THE BRUECKNER HARTREE-FOCK METHOD

The realistic NN interaction cannot be directly applied to exactly describe nuclear many-body systems, such as finite nuclei and infinite nuclear matter within the independent-particle approximation. It should be normalized to treat the strong repulsion at short-range and take three-body force into account in a non-relativistic framework. An available renormalization method was named as Brueckner Hartree-Fock (BHF) method, where an effective interaction G will replace of the realistic NN interaction, V within the Bethe-Goldstone equation [52],

$$G(\omega, k_F) = V + \sum_{k_1, k_2 > k_F} V \frac{Q(k_1, k_2)}{\omega - \varepsilon_1(k_1) - \varepsilon_2(k_2) + i\epsilon} G(\omega, k_F), \quad (30)$$

where k_F is the Fermi momentum of the nucleon, ω is the starting energy, $Q(k_1, k_2)$ is the Pauli exclusion operator, and $\varepsilon(k)$ is the single-particle energy given as,

$$\begin{aligned} \varepsilon(k) &= \frac{k^2}{2M_N} + U(k; k_F) \\ &= \frac{k^2}{2M_N} + Re \sum_{k' \leq k_F} \langle kk' | G(\varepsilon_1(k_1) + \varepsilon_2(k_2), k_F) | kk' \rangle_A. \end{aligned} \quad (31)$$

The subscript of A indicates the anti-symmetry wave function. When the normalized interaction G is applied in the Hartree-Fock approximation, the energy per nucleon of nuclear matter can be shown as,

$$B/A = \frac{3k_F^2}{10M_N} + \frac{1}{2\rho} \sum_{k,k' \leq k_F} \text{Re} \langle kk' | G(\varepsilon_1(k_1) + \varepsilon_2(k_2), k_F) | kk' \rangle_A. \quad (32)$$

In the last part, the EOS of nuclear matter is calculated in the framework of the BHF method, with different two-body high-precision NN potentials. The symmetric nuclear matter case is shown in the upper panel of Fig. 8. The binding energy per nucleon monotonically decreases with baryon density rising below $\rho < 0.2 \text{ fm}^{-3}$. The EOSs from N⁴LO (EMN) and N⁴LO (RKE) do not have the saturation character before $\rho = 0.5 \text{ fm}^{-3}$, since they are very soft at short-range region. While another chiral potential, N⁴LO (EKM) is regularized in the coordinate space, it becomes harder and can generate the saturation point. The other non-chiral potentials also can provide the saturation points around $\rho_{sat} = 0.25\text{-}0.35 \text{ fm}^{-3}$, which are a little far from the empirical data around $\rho_{sat} = 0.16 \text{ fm}^{-3}$. The repulsive contribution of three-body force is required in the non-relativistic framework to provide the reasonable saturation properties of symmetric nuclear matter.

The EOSs of pure neutron matter are plotted in the lower panel of Fig. 8. All of them monotonically increase with density and are almost identical below the empirical saturation density. The differences become significant above $\rho = 0.20 \text{ fm}^{-3}$. The softer chiral potentials, N⁴LO (EMN) and N⁴LO (RKE), still have the lowest binding energy. The AV18 and N⁴LO 0.8(EKM) contribute to the stiffer EOSs. Furthermore, it can be found that the regularized cut-off momentum in N⁴LO (REK) has the smallest influence on the EOS, while that in N⁴LO 0.8(EKM) has a very strong effect.

VI. CONCLUSIONS

In this work, the high-precision NN interaction potentials proposed in recent years, including AV18 potential, CD-Bonn potential, chiral potentials, and pvCD-Bonn potentials, were compared with each other from the aspects of phase shifts, differential cross sections, entanglement powers, and EOSs of symmetric nuclear matter and pure neutron matter.

It was found that the phase shifts from chiral potentials have obvious differences in contrast to the partial wave analysis from the experimental data and other meson-exchange

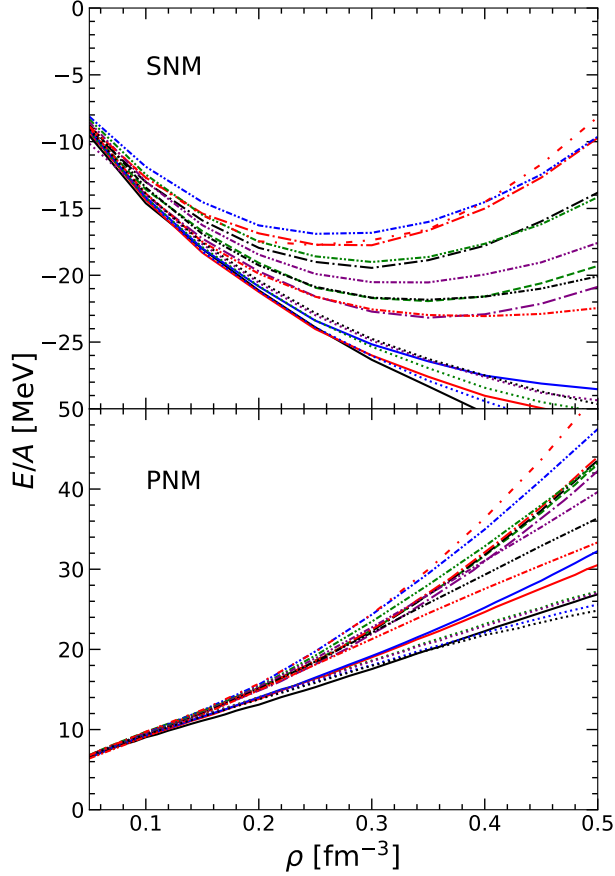


FIG. 8. The energy per nucleon as a function of the density of symmetric nuclear matter and pure neutron matter with different NN potentials in the framework of Brueckner-Hartree-Fock method. The meanings of line styles are same as Fig. 7.

potentials for the high partial wave channels at high input energy region. This is because the number of low energy constants in chiral potentials is limited by the perturbation order. Low-energy constants at order Q^4 are just determined by the D -state channel. Therefore, the phase shifts at the F channel are the predicted values. Furthermore, the regularized cut-off in the chiral potentials also has a non-negligible effect. In addition, the mixing angles between 3S_1 and 3D_1 channels from various NN potentials are also quite distinguished, which are not observable in NN scattering.

The differential cross sections from these potentials for the pp scattering below $E_{lab} = 100$ MeV are consistent with each other and produce the experimental data perfectly at the scattering angle from 0 to π . Whereas, there are obvious differences around $\theta_{cm} = 0$ and $\theta_{cm} = \pi$ once $E_{lab} > 200$ MeV. Especially, the descriptions of chiral potentials on observables

become worse, which should be related to poor phase shifts at high partial waves. All of these potentials produced a similar entanglement power for np scattering at 1S_0 and 3S_1 channels. Their spins flip around input momentum $p = 14$ MeV. At very high momentum region, the entanglement power from N⁴LO 550(EMN) potential is lower than others.

The equations of state of infinite nuclear matter from these potentials have similar behaviors below the nuclear saturation density in the framework of the BHF method. As the density increases, the differences among high-precision nuclear interactions become obvious. The chiral potentials with momentum regulators are very soft so that there are no saturation points for symmetric nuclear matter before nuclear density $\rho < 0.5$ fm⁻³. However, the saturation properties from other potentials are far from the empirical data, indicating that the extra repulsive contributions from the three-body force are required.

Although the high-precision NN potentials were claimed to describe the scattering observables with an accuracy of $\chi^2/N \sim 1$, they are still quite distinct in high-energy and high-density regions. It is necessary to reduce their uncertainties in these extreme conditions so that we can apply them to the investigations on the nuclear many-body system.

VII. ACKNOWLEDGMENTS

This work was supported in part by the National Natural Science Foundation of China No. 12175109, the Natural Science Foundation of Tianjin (Grant No: 19JCYBJC30800), and the Natural Science Foundation of Guangdong Province (Grant No: 2024A1515010911).

-
- [1] E. Epelbaum, H. W. Hammer, and U.-G. Meißner, *Rev. Mod. Phys.* **81** (2009) 1773.
- [2] R. Machleidt and D. R. Entem, *Phys. Rep.* **503** (2011) 1.
- [3] H. Yukawa, *Proc. Phys. Math. Soc. Jpn.* **17** (1935) 48.
- [4] K. Erkelenz, *Phys. Rep.* **13** (1974) 191 .
- [5] R. Machleidt, K. Holinde, and Ch. Elster, *Phys. Rep.* **149** (1987) 1.
- [6] R. Machleidt, *Adv. Nucl. Phys.* **19** (1989) 189.
- [7] V. G. J. Stoks, R. A. M. Klomp, C. P. F. Terheggen, and J. J. de Swart, *Phys. Rev. C* **49** (1994) 2950.
- [8] R. B. Wiringa, V. G. J. Stoks, and R. Schiavilla, *Phys. Rev. C* **51** (1995) 38 .
- [9] R. Machleidt, *Phys. Rev. C* **63** (2001) 024001.
- [10] S. Weinberg, *Phys. Lett. B* **251** (1990) 288 .
- [11] S. Weinberg, *Nuclear Phys. B* **363** (1991) 3.
- [12] S. Weinberg, *Phys. Lett. B* **295** (1992) 114.
- [13] C. Ordóñez, L. Ray, and U. van Kolck, *Phys. Rev. Lett.* **72** (1994) 1982.
- [14] C. Ordóñez, L. Ray, and U. van Kolck, *Phys. Rev. C* **53** (1996) 2086.
- [15] E. Epelbaum, W. Glöckle, and U.-G. Meißner, *Nucl. Phys. A* **637** (1998) 107.
- [16] E. Epelbaum, W. Glöckle, and U.-G. Meißner, *Nucl. Phys. A* **671** (2000) 295.
- [17] D. R. Entem and R. Machleidt, *Phys. Rev. C* **68** (2003) 041001(R).
- [18] E. Epelbaum, W. Glöckle, and U.-G. Meißner, *Nucl. Phys. A* **747** (2005) 362.
- [19] D. R. Entem, N. Kaiser, R. Machleidt, and Y. Nosyk, *Phys. Rev. C* **91** (2015) 014002.
- [20] E. Epelbaum, H. Krebs, and Ulf.-G. Meißner, *Eur. Phys. J. A* **51** (2015) 1.
- [21] E. Epelbaum, H. Krebs, and Ulf.-G. Meißner, *Phys. Rev. Lett.* **115** (2015) 122301.
- [22] D. R. Entem, R. Machleidt, and Y. Nosyk, *Phys. Rev. C* **96** (2017) 02400.
- [23] P. Reinert, H. Krebs, and E. Epelbaum, *Eur. Phys. J. A* **54** (2018) 1.
- [24] X. L. Ren, K. W. Li, L. S. Geng, B. W. Long, P. Ring, and J. Meng, *Chin. Phys. C* **42** (2018) 014103.
- [25] Y. Xiao, L.-S. Geng, and X.-L. Ren, *Phys. Rev. C* **99** (2019) 024004 (2019).
- [26] J. X. Lu, C. X. Wang, Y. Xiao, L. S. Geng, J. Meng, and P. Ring, *Phys. Rev. Lett.* **128** (2022) 142002.

- [27] W. J. Zou, J. X. Lu, P. W. Zhao, L. S. Geng, and J. Meng. Phys. Lett. B **854** (2024) 138732.
- [28] R. Navarro Pérez, E. Garrido, J.E. Amaro, and E. Ruiz Arriola, Phys. Rev. C **90** (2014) 047001.
- [29] E. Ruiz Arriola, J. E. Amaro, and R. Navarro Pérez, Front. Phys. **8** (2020) 1.
- [30] N. Ishii, S. Aoki, and T. Hatsuda, Phys. Rev. Lett. **99** (2007) 022001.
- [31] T. Inoue, N. Ishii, S. Aoki et al., Phys. Rev. Lett. **106** (2011) 162002.
- [32] S. R. Beane, E. Chang, S. D. Cohen et al., Phys. Rev. C **88** (2013) 024003.
- [33] C. McIlroy, C. Barbieri, T. Inoue et al., Phys. Rev. C **97** (2018) 021303(R).
- [34] Y. Lyu, H. Tong, T. Sugiura, S. Aoki, T. Doi, T. Hatsuda, J. Meng, and T. Miyamoto Phys. Rev. Lett. **127** (2021) 072003.
- [35] Y. Lyu, S. Aoki, T. Doi, T. Hatsuda, Y. Ikeda, and J. Meng, Phys. Rev. Lett. **131** (2023) 161901.
- [36] J. Hu, H. Toki, and H. Shen, Sci. Rep. **6** (2016) 35590.
- [37] J. Song, K. W. Li, and L. S. Geng, Phys. Rev. C **97** (2018) 065201.
- [38] Q. Q. Bai, C. X. Wang, Y. Xiao, L. S. Geng, Phys. Lett. B **809** (2020) 135745.
- [39] J. Hu, Y. Zhang, H. Shen, and H. Toki, Chin. Phys. C **44** (2020) 071002.
- [40] N. L. Harshman, Int. J. Mod. Phys. A, **20** (2005) 6220.
- [41] S. R. Beane, D. B. Kaplan, Natalie Klco, and Martin J. Savage, Phys. Rev. Lett. **122** (2019) 102001.
- [42] I. Low and T. Mehen, Phys. Rev. D **104** (2021) 074014.
- [43] D. Bai, Phys. Lett. B **845** (2023) 138162.
- [44] T. R. Hu, S. Chen, and F. K. Guo, arXiv:2404.05958.
- [45] G. Caia, J. W. Durso, Ch. Elster, J. Haidenbauer, A. Sibirtsev, and J. Speth, Phys. Rev. C **66** (2002) 044006.
- [46] M. Lacombe *et al.*, Phys. Rev. D **12** (1975) 1495.
- [47] A. D. Jackson, D. O. Riska, and B. Verwest, Nucl. Phys. A **249** (1975) 397 .
- [48] S. K. D. Drechsel and L. Tiator, J. Phys. G **18** (1992) 449.
- [49] S. K. D. Drechsel, O. Hanstein, and L. Tiator, Nucl. Phys. A **645** (1999) 145.
- [50] C. Fuchs, T. Waindzoeh, A. Faessler, and D. S. Kosov, Phys. Rev. C **58** (1998) 2022 .
- [51] R. Brockmann and R. Machleidt, Phys. Rev. C **42** (1990) 1965 .
- [52] J. Hu, Y. Zhang, E. Epelbaum, Ulf.-G. Meißner, and J. Meng, Phys. Rev. C **96** (2017) 034307.

- [53] S. Shen, H. Liang, W. Long, J. Meng, and P. Ring, *Prog. Part. Nucl. Phys.* **109** (2019) 103713.
- [54] C. Wang, J. Hu, Y. Zhang, and H. Shen, *J. Phys. G* **47** (2020) 105108 .
- [55] C. Wang, J. Hu, Y. Zhang, and H. Shen, *Chin. Phys. C* **43** (2019) 114107 .
- [56] M. Haftel and F. Tabakin, *Nucl. Phys. A*, **158** (1970) 1.
- [57] J. Blatt and L. Biedenharn, *Phys. Rev.* **86** (1952) 399 .
- [58] H. P. Stapp, T. J. Ypsilantis, and N. Metropolis, *Phys. Rev.* **105** (1957) 302.
- [59] R. J. Furnstahl, N. Klco, D.R. Phillips, S. Wesolowski, *Phys. Rev. C* **92** (2015)024005.
- [60] J. A. Melendez, S. Wesolowski, R.J. Furnstahl, *Phys. Rev. C* **96** (2017) 024003.
- [61] J. A. Melendez, R. J. Furnstahl, D. R. Phillips, M. T. Pratola, and S. Wesolowski, *Phys. Rev. C* **100** (2019) 044001.
- [62] L. Wolfenstein, *Ann. Rev. Nucl. Part. Sci.* **6** (1956) 43.
- [63] N. Hoshizaki, *Prog. Theor. Phys. Suppl.* **42** (1969) 107.
- [64] J. Bystricky, F. Lehar, and P. Winternitz, *J. Phys.(France)* **39** (1978) 1.
- [65] Q. F. Liu and I. Low, *Phys. Lett. B* **856** (2024) 138899.
- [66] D. Bai, *Phys. Rev. C* **109** (2024) 034001.